Ceria-supported small Pt and Pt₃Sn nanoparticles for NOₓ-assisted soot oxidation

Tahrizi Andana [a,b], Marco Piumetti [a], Samir Bensaid [a,*], Laurent Veyre [b], Chloé Thieuleux [b], Nunzio Russo [a], Debora Fino [a], Elsje Alessandra Quadrelli [b], Raffaele Pirone [a]

[a] Department of Applied Science and Technology, Politecnico di Torino, Corso Duca degli Abruzzi 24, 10129 Turin, Italy
[b] Universiteí de Lyon, ICL, C2P2 UMR 5265, CPE Lyon, 43 Bd du 11 Novembre 1918, F-69616 Villeurbanne, France

ABSTRACT

Introduced herein are small Pt and Pt₃Sn nanoparticles, stabilized with organosilane or organostannane and impregnated on ceria support, as active sites for NOₓ-assisted soot oxidation reaction. The catalysts have been tested with four reactions: CO oxidation, NO oxidation, NOₓ-free soot oxidation and finally NOₓ-assisted soot oxidation. Our Pt nanoparticles reportedly possess remarkable catalytic activities in CO oxidation, as they actively convert CO at 50 °C, while the alloy Pt₃Sn nanoparticles are active at higher temperature. The Pt nanoparticles also mediate more actively NO oxidation than their alloy counterpart, leading to more NO₂ production beneficial for soot oxidation. The influence of Pt and Pt₃Sn active sites on the catalytic activity during NOₓ-free soot oxidation becomes less prominent than the morphology, due to the high dependency of the reaction on catalyst structure. The presence of Sn, nevertheless, induces lower oxidation reaction temperature. Finally, in the presence of NOₓ, the metal active sites undoubtedly boost the catalytic activity of soot oxidation. Pt/CeO₂-NC (NC stands for "nanocubes"), reported herein as our most achieving catalyst, demonstrates a remarkable activity, lowering the oxidation temperature at about 80 °C, thanks to the synergy of the active metal nanoparticles and reactive ceria nanocubes. Surprisingly, the catalytic activity of the alloy counterpart (Pt₃Sn/CeO₂-NC) is close to Pt/CeO₂-NC, indicating the potential of the catalyst as an alternative to reducing the employment of precious metal in automotive catalysis. The thermally aged Pt catalysts have demonstrated good resistance to sintering, thanks to the outer protection by silica patches. However, the catalytic activities of the aged Pt₃Sn catalysts rely heavily on support morphology.

1. Introduction

Diesel exhaust gas aftertreatment technology has been experiencing years of developments. New challenges for current car manufacturers have emerged since the enforcement of Euro VI, in which emissions of particulate matter (PM) and nitrogen oxides (NOₓ) must be reduced till 0.005 and 0.08 g km⁻¹, respectively [1]. Obsolete reduction technologies involving modifications in an internal combustion engine are no longer efficient in yielding very low pollutant emissions. Therefore, downstream pollutant abatement involving approaches from chemistry and catalysis must unavoidably be taken.

Particulate matter (PM), more colloquially called "soot", has been an ongoing issue in developing Diesel engine vehicles due

to its detrimental impact on respiratory system [2]. Constituted mainly of carbonaceous compounds, soot can solely be abated via oxidation reactions. Due to its solid nature, soot is normally treated in two steps: filtration and regeneration. The former refers to the entrapment of soot in a Diesel Particulate Filter (DPF); a porous, monolithic structure that enables wall-flow filtration [3,4]. The latter refers to the cleanup of soot-laden filter via combustion in order to avoid the entailing backpressure. Regenerating filter is a demanding task as oftentimes the reaction condition may become too extreme. In a conventional fashion, the regeneration is carried out in "active" mode [5–7], which requires active participation from oxygen, active thermal induction coming from Diesel Oxidation Catalyst (DOC), and a catalytic washcoat. The reaction between soot and oxygen, even mediated with catalysts, occurs effectively at above 550 °C [3,6,7]. The exothermicity of the reaction, however, could raise the overall temperature up to 1000 °C, inflicting structural damage to the filter. The contemporary approach, known as "passive regeneration" [6–8], involves NOₓ as the third reagent,
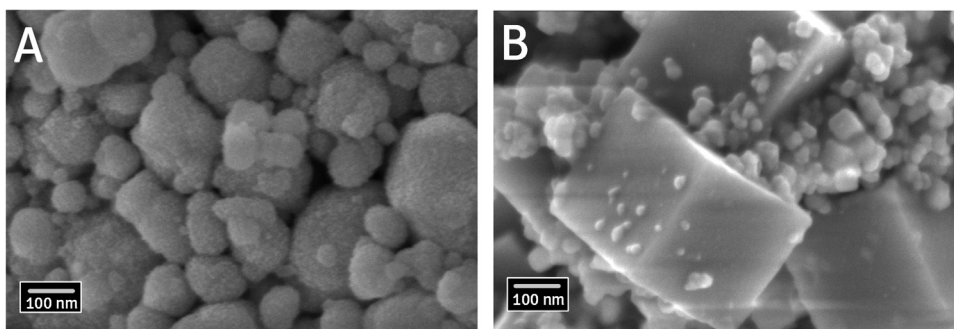
Fig. 1. FE-SEM images of catalyst's supports: (A) CeO_2-SCS and (B) CeO_2-NC.

thanks to its abundant presence in Diesel exhaust gas stream. This NO_x-assisted reaction benefits from the strong oxidizing nature of NO_2, with which soot combustion is expected to occur at lower temperature. Two major components constituting a perfect catalyst for passive regeneration are: (1) an oxide support and (2) an active oxidation catalyst

Cerium dioxide (CeO_2), casually known as "ceria", has been popular amid global researchers for its ability to undergo rapid reduction and oxidation (its so-called "redox properties") and to have outstanding oxygen storage capacity (OSC), therefore it is frequently studied as the potential oxide support [9–15]. Many researchers have been investigating the effect of various physico-chemical properties of ceria in order to obtain not only better soot oxidation [16–23] but also better CO and propane oxidation [24]. Tailoring the right morphology of ceria, in particular, could induce high catalytic activity, as catalytic soot oxidation strongly necessitates a good interaction between soot, a solid reactant, and the solid-phase catalyst [25,26]. Interestingly, various shapes often give different reactivity towards the reaction, especially in the nanoscale level. Previous research, taken as examples, have demonstrated that well-defined ceria nanocubes and nanorods enhance soot oxidation activity compared to ceria nanopolyhedra, owing to their reactive, rather unstable (100) and (110) planes [16,17,19].

Platinum-Group Metals (PGMs) are broadly used as active oxidation catalysts. Besides their remarkable activities for any oxidation reactions, PGMs are still preferred because of their resistance to corrosion. Platinum (Pt), in particular, has been employed in many automotive catalytic processes, starting from Diesel Oxidation Catalysts (DOC) [27,28], the early generation of catalytic converters, to Three-Way Catalysis (TWC) [29] for abating simultaneously CO, hydrocarbons and NO_x emissions through oxidation-reduction cycles and the most recent Lean NO_x Trap (LNT) [30,31], in which NO_x are periodically trapped and reduced to N_2. The activity of Pt-containing phase relies much on its particle size; the smaller the size, the better the oxidation activity [32,33]. However, since automotive catalysis normally runs at high temperatures under oxidative atmosphere, Pt often suffers from sintering – particle enlargement via diffusion/agglomeration or ripening process [34–36]. As the particle loses its active sites, sintering leads to catalyst deactivation. Stabilized Pt nanoparticles are an alternative to the conventional, large Pt clusters and they are prepared via an organometallic synthesis [37–39]. Pelzer et al. have successfully obtained small (± 2 nm) Pt(0) nanoparticles, stabilized with n-octylsilane via direct Pt_3Si bonds [38]. The silyl ligands not only help prevent Pt nanoparticles from agglomeration during particle growth but also keep them from sintering when they are already impregnated onto a support.

Commercialization of Pt-based automotive catalysts, however, remains an issue due to the prohibitive price of the metal. A possible alternative to this might be a dilution of Pt with non-noble metals. Interestingly, the alloy Pt_3Sn can be prepared through the same organometallic synthesis [40]. Boualleg et al. have observed an unexpected formation of Pt_3Sn nanoparticles after contacting Pt and Sn precursors [Pt(dba)$_2$ (dba = dibenzylideneacetone) and (n-Bu)$_3$Sn-H] under H_2 at room temperature without using other stabilizing ligands [40].

The present work reports such small Pt and Pt_3Sn nanoparticles impregnated onto ceria nanocubes (prepared via a hydrothermal synthesis) as a new means of mediating low-temperature NO_x-assisted soot abatement. Four reactions have been carried out to shed light on the performances of the prepared catalysts: (1) CO oxidation as an intermediate reaction in the mechanism of soot oxidation; (2) NO oxidation as the reaction that helps understand the functionality of Pt nanoparticles in producing NO_2; (3) regular soot oxidation under oxygenic atmosphere as the core reaction in the present study; and eventually (4) soot oxidation in the presence of NO_x. Another ceria support, synthesized through solution combustion technique, has also been used for comparison. This work is finally completed with several catalyst characterizations.

2. Experimental

2.1. Catalyst preparation

Two cerium dioxide supports, namely CeO_2-SCS (SCS = solution combustion synthesis) and CeO_2-NC (NC = nanocubes) have been prepared through solution combustion and hydrothermal syntheses respectively. In a typical SC synthesis, Ce(NO$_3$)$_3$·6H$_2$O (4 mmol, Sigma-Aldrich) and CO(NH$_2$)$_2$ (10 mmol, Sigma-Aldrich) are dissolved in 60 ml of deionized H$_2$O. The solution is then transferred into a ceramic crucible, heated in a furnace at 650 °C for 20 min. On the other hand, a typical hydrothermal synthesis requires precipitating 0.01 mmol of Ce(NO$_3$)$_3$·6H$_2$O (0.01 mmol) with NaOH (1.2 mol, Sigma-Aldrich), in 80 ml of deionized water. The violetish-white slurry resulting from the precipitation is then transferred into a 200-ml autoclave, heated at 180 °C for 24 h. The clear white precipitate is rinsed with ethanol and deionized water, separated from the washing liquid in a centrifuge and dried overnight at 70 °C. The final dried precipitate is calcined at 550 °C for 4 h.

In the synthesis of the Pt and Pt_3Sn nanoparticles, Pt(dba)$_2$ is used as the precursor and prepared according to the literature [41]. Pt nanoparticles were obtained as a dark brown colloid (0.05 mmol) by contacting Pt(dba)$_2$ (0.05 mmol) and Si(n-C$_8$H$_{17}$) (Sigma-Aldrich) (0.05 mmol) in dry THF (34 ml) in a Schlenk flask under Ar which is then transferred to a high-pressure glass reactor for a reaction under 3 bar of H_2. Pt_3Sn nanoparticles (0.04 mmol) were obtained likewise by contacting Pt(dba)$_2$ (0.04 mmol) with (n-Bu)$_3$Sn-H (Sigma-Aldrich) (0.04 mmol, excess), in dry THF (28 ml). The excess of Sn, in the synthesis of Pt_3Sn nanoparticles, is removed by three-time washings with dry pentane, followed by cryogenic precipitation and decantation (liquid nitrogen as coolant).

Table 1
BET specific surface areas (S_{BET}), total pore volumes ($V_{p,t}$) and platinum content of the prepared samples.

Sample	S_{BET} ($m^2\,g^{-1}$)[a]	$V_{p,t}$ ($cm^3\,g^{-1}$)[a]	Pt content (%-wt)[b]
CeO$_2$-SCS	38	0.04	–
CeO$_2$-NC	8	0.07	–
Pt/CeO$_2$-SCS	28	0.03	0.88
Pt/CeO$_2$-NC	8	0.03	0.87
Pt$_3$Sn/CeO$_2$-SCS	33	0.03	0.22
Pt$_3$Sn/CeO$_2$-NC	8	0.03	0.74

[a] Obtained from N$_2$ physisorption at $-196\,^\circ$C.
[b] Obtained from ICP-AES.

Table 2
Comparison of experimental and theoretical Pt$_3$Sn crystal parameters obtained from FFT image analysis.

Parameters	Experimental	Theoretical
$d_{h,k,l}$ (nm) (h,k,l)		
Spot 1	0.284 (1,1,0)	0.283 (1,1,0)
Spot 2	0.208 (2,0,0)	0.200 (2,0,0)
Spot 3	0.284 (1,−1,0)	0.283 (1,−1,0)
Spot 4	0.204 (0,−2,0)	0.200 (0,−2,0)
Angle ($^\circ$)		
Spot 1	0	0
Spot 2	45.77	45
Spot 3	91.20	90
Spot 4	134.17	135

1%-wt loading, with respect to the weight of supports, of Pt or Pt$_3$Sn nanoparticles onto cerium dioxide supports have been achieved by wetness impregnation (WI). The final colloid of Pt or Pt$_3$Sn nanoparticles is concentrated via vacuum evaporation till the adequate volume is reached. The concentrated colloid is carefully impregnated dropwise onto the support under flowing Ar. The wet support is left overnight under air at ambient temperature to allow drying. Finally, the Pt- or Pt$_3$Sn-impregnated support is air-dried at 120 $^\circ$C for 2 h to remove the remaining solvent and then calcined at 320 $^\circ$C for 10 h to remove the ungrafted ligands.

2.2. Catalyst characterization

BET surface areas and pore volumes have been obtained from nitrogen physisorption analysis, performed by a Tristar II 3020 Micromeritics instrument at Politecnico di Torino, Turin, Italy. Catalyst pretreatment was done by heating the catalyst at 200 $^\circ$C for 2 h. BET method was applied to calculate the specific surface area of the catalyst. Platinum content determination in all of the prepared catalysts was carried out via elemental analyses in an ICP-AES instrument at "Mikroanalytisches Labor Pascher" in Germany.

The morphology of ceria supports was observed through a field emission scanning electron microscopy, using a FESEM Zeiss MER-LIN, Gemini-II column at Politecnico di Torino, Turin, Italy while the morphology of the colloids and impregnated catalysts was investigated in High Resolution Transmission Electron Microscopy (HRTEM) using a MET JEOL 2100FEG (field emission gun) microscope at the "Centre Technologique des Microstructures", CTµ, Villeurbanne, France, equipped with an energy-dispersive x-ray (EDX) analyzer

Oxidation states of Ce, O and Pt on the surface level were deduced from the interpretation of deconvoluted X-ray photoelectron spectra produced by PHI Versa probe apparatus using a band-pass energy of 187.85 eV, a 45° take off angle and a 100.0 µm diameter X-ray spot size.

2.3. Catalytic activity tests

The tests of the prepared catalysts have been designed as a classical temperature-programmed oxidation (TPO). A typical setup of TPO comprises a quartz U-tube fixed-bed reactor, a PID-regulated furnace, a K-type thermocouple placed as close as possible to the catalytic bed, a non-dispersive infrared (NDIR) continuous gas analyzer (ABB Uras 14) for NO, CO and CO$_2$ detection and an Emerson XStream X2GP gas analyzer for NO$_2$ and O$_2$ detection.

In *CO oxidation* tests, the catalytic bed consists of 100 mg of catalyst. The catalyst is pre-treated with 50 ml min^{-1} of air at 100 $^\circ$C for 30 min. Then, the reactor is ramp-cooled (5 $^\circ$C min^{-1}) to 50 $^\circ$C, followed by CO flow admission (50 ml min^{-1} of a mixture of 1000 ppmv CO and 10%-v O$_2$ in N$_2$). The isothermal reaction at 50 $^\circ$C is performed at the beginning to observe possible CO conversion. After the saturation, the programmed heating ramp (5 $^\circ$C min^{-1}) is activated and the test continues till 100 percent CO conversion.

In *NO oxidation* tests, the catalytic bed is comprised of 150 mg of SiO$_2$ and 45 mg of catalyst, gently mixed with a spatula for 3 min. The catalyst is pre-treated with 100 ml min^{-1} of 20%-v O$_2$ in N$_2$ at 100 $^\circ$C for 30 min. Then, the reactor is ramp-cooled (5 $^\circ$C min^{-1}) to 50 $^\circ$C, followed by NO flow admission (100 ml min^{-1} of a mixture of 550 ppmv NO and 10%-v O$_2$ in N$_2$) till the stabilization of the gas concentrations. The tests were carried out in two modes: (1) ramping; and (2) stepwise isothermal. In the former case, the reactor is heated at a programmed rate of 5 $^\circ$C min^{-1} from 50 to 650 $^\circ$C. In the latter case, the reactor is heated stepwise by 5 $^\circ$C, followed by an isothermal treatment at the corresponding temperature till the stabilization of the gas concentrations. The heating is also performed from 50 to 650 $^\circ$C.

In regular *soot oxidation* tests, the catalytic bed contains 150 mg of SiO$_2$, 45 mg of catalyst and 5 mg of soot (Printex-U from Degussa), gently mixed with a spatula for 3 min to achieve "loose" contact. The catalyst is initially pre-treated with 100 ml min^{-1} of N$_2$ at 100 $^\circ$C for 30 min and then with 100 ml min^{-1} of a mixture of 10%-v O$_2$ in N$_2$ at the same temperature for 30 min. Then, the reactor is heated gradually at a rate of 5 $^\circ$C min^{-1} to 700 $^\circ$C.

In *NO$_x$-assisted soot oxidation* tests, the catalytic bed contains 150 mg of SiO$_2$, 45 mg of catalyst and 5 mg of soot (Printex-U from Degussa), gently mixed with a spatula for 3 min to achieve "loose" contact. The catalyst is pre-treated with 100 ml min^{-1} of 20%-v O$_2$ in N$_2$ at 100 $^\circ$C for 30 min. Then, the reactor is ramp-cooled (5 $^\circ$C min^{-1}) to 50 $^\circ$C, followed by NO flow admission (100 ml min^{-1} of a mixture of 550 ppmv NO and 10%-v O$_2$ in N$_2$). After the stabilization of NO$_x$ concentrations, the reactor is heated gradually at a rate of 5 $^\circ$C min^{-1} to 700 $^\circ$C.

Finally, the stability of platinum/platinum-tin nanoparticles against sintering is confirmed via tests with used and aged catalysts. The used catalysts are obtained by recovering the catalysts that have been tested once with NO$_x$-assisted soot oxidation reaction. This stability test is further named "second cycle". The aged catalysts are obtained by heating the catalysts at 700 $^\circ$C for 8 h in a furnace. Each test uses exactly the same procedure and reactor

Table 3
Relative abundances of cerium species derived from the deconvolution of Ce $3d$ XP spectra.

Sample	Ce $3d_{5/2}$							
	Ce(IV)						Ce(III)	
	BE (eV)	%-atom	BE (eV)	%-atom	BE (eV)	%-atom	BE (eV)	%-atom
Pt/CeO$_2$-SCS	882.5	8.9	889.1	13	898.5	20	883.7	22
Pt/CeO$_2$-NC	882.1	10	888.5	15	898.0	21	883.2	16
Pt$_3$Sn/CeO$_2$-SCS	882.2	9.6	888.9	11	898.2	20	883.6	24
Pt$_3$Sn/CeO$_2$-NC	881.9	8.8	888.5	14	897.8	21	882.8	18
CeO$_2$-SCS	882.3	8.3	889.0	12	898.4	19	883.5	22
CeO$_2$-NC	882.2	10	888.8	13	898.1	20	883.5	14

Sample	Ce $3d_{3/2}$							
	Ce(IV)						Ce(III)	
	BE (eV)	%-atom	BE (eV)	%-atom	BE (eV)	%-atom	BE (eV)	%-atom
Pt/CeO$_2$-SCS	901.1	8.1	907.6	8.5	916.9	14	902.5	5.8
Pt/CeO$_2$-NC	900.6	8.4	907.3	9.2	916.4	15	902.0	5.1
Pt$_3$Sn/CeO$_2$-SCS	900.8	7.7	907.4	6.0	916.6	13	902.4	7.8
Pt$_3$Sn/CeO$_2$-NC	900.4	7.9	907.2	11	916.2	15	901.7	5.2
CeO$_2$-SCS	900.9	7.7	907.4	11	916.7	14	902.3	7.0
CeO$_2$-NC	900.7	7.4	907.7	12	916.5	16	902.0	6.7

procedure with the ones for NO$_x$-assisted soot oxidation tests (see previous paragraph for more details).

3. Result and discussion

3.1. Catalyst characterization

Nitrogen physisorption analysis has been carried out to determine BET specific surface areas and total pore volumes of the samples and their values are summarized on Table 1. The CeO$_2$-SCS sample has a specific surface area nearly five times higher than CeO$_2$-NC. This signifies the presence of more abundant intraparticle voids in the SC-synthesized sample. Impregnation with Pt and Pt$_3$Sn nanoparticles lowers the surface area of the CeO$_2$-SCS catalyst as they partially occupy the surfaces. However, in the case of nanocubic ceria, the impregnation with Pt and Pt$_3$Sn hardly changes the specific surface area. Results from elemental analysis by ICP-AES (see Table 1) have shown that the Pt contents in most catalysts are around 0.7–0.8 percent, in a good agreement with the intended metal loading.

Fig. 1 shows FE-SEM images of the supports: CeO$_2$-SCS (Fig. 1A) and CeO$_2$-NC (Fig. 1B). In general, the CeO$_2$-SCS sample exhibits clusters of globular agglomerates whose maximum size is around 100 nm. The foamy structure of the sample is typically obtained via solution combustion synthesis as a large amount of gas is rapidly emitted during the reaction [42,43]. Hydrothermal synthesis, on the other hand, results in well-defined nanostructures since the process is tunable with three parameters: temperature, basicity and aging time. A well-defined nanocube with smooth surfaces is obtained by applying high temperature, highly basic medium and long aging time since this condition is necessary to form high energy (100) surfaces [44]. The size of the nanocubes in the sample ranges from 100 to 300 nm; such a large dimension is due to the synthesis condition that also favors Ostwald ripening [44].

TEM images of colloidal Pt and Pt$_3$Sn nanoparticles (NPs) are shown on Fig. 2A and B respectively and their corresponding size distributions are shown on Fig. 2C and D. It is evident that the stabilization of Pt NPs with organosilane results in a narrow particle size distribution (Fig. 2C), ranging from 0.5 to 1.5 nm, while the Pt–Sn alloy NPs are present in a wider spectrum, ranging from 0.5 to 2.5 nm. The three unstable Si—H bonds in *n*-octylsilane are cleft easily, capturing Pt via Pt$_3$(η^3-≡Si) bonds. It is also known that Si—C bond in *n*-octylsilane is stronger than the Sn—C bond toward

hydrogenolysis, therefore the use of silanes is perfect for keeping the organometallic fragments at the surface of metal particles [45]. Fig. 2F shows the HRTEM image of a single Pt$_3$Sn nanoparticle while Fig. 2E shows its FFT-processed image. Four diffraction spots have been selected (indexed with numbers) for determining their Miller indices (h,k,l) and their interplanar spacing ($d_{h,k,l}$) with respect to the diffractogram center. Table 2 summarizes the $d_{h,k,l}$ of four selected diffraction spots and their corresponding diffraction angles. The theoretical values are presented therein for comparison. The values of $d_{h,k,l}$ obtained from the experiment seem approaching the theoretical ones, with a minor difference (0.001–0.008 nm). The same trend is equally observed in the experimental data of diffraction angles, with the difference at approximately 1°. This closeness has confirmed that Pt$_3$Sn alloy was spontaneously formed during the reaction between Pt(dba)$_2$ precursor and trialkyltin hydride.

Fig. 3 shows the TEM images of all Pt-containing samples. CeO$_2$-SCS, as seen on Fig. 3A, typically appears as a polycrystalline material with pronounced lattice fringes. The strong topological feature of CeO$_2$-SCS limits the distinction of impregnated Pt-NPs on the surface as dark, high density zones predominate. Therefore, zones with lower thickness at support's edges are picked. On Fig. 3B, it is observed that the particles appear as spheres well-deposited onto the selected surface of CeO$_2$-SCS. The size of the particles is between 1.6–2 nm, slightly bigger than their size in the colloidal solution. Fig. 3C shows the image of Pt/CeO$_2$-SCS, magnified lower than the previous images of Pt/CeO$_2$-SCS in order to best capture ceria nanocubes that are generally large in dimension. Having rather smooth surfaces and well-defined shapes, the deposition of Pt-NPs onto CeO$_2$-NC is clearly observed. The small, spherical Pt-NPs are deposited homogeneously on CeO$_2$-NC surfaces. Fig. 3D shows higher magnification of the selected area on Fig. 3C. From the image, particles of 2–2.5 nm in size dominate while smaller particles (1.5–1.6 nm) also exists. Fig. 3E and F show the images of Pt$_3$Sn/CeO$_2$-SCS, in which it shares morphological similarity with Pt/CeO$_2$-SCS. However, in this sample the presence of Pt$_3$Sn-NPs is somewhat scarce. Only in certain regions, including the one captured on Fig. 3F the particles are well observed (size at about 2–2.3 nm). Fig. 3G and H show the images of Pt$_3$Sn/CeO$_2$-NC. The deposition of Pt$_3$Sn-NPs is quite homogeneous on the smooth surface of the nanocubes. The size of the particles is between 1.8–2.5 nm. A small inset on Fig. 3H shows the magnified image of a single Pt$_3$Sn particle (the selected zone marked by a small dashed square). Analysis of interplanar spacing in this particle, carried out
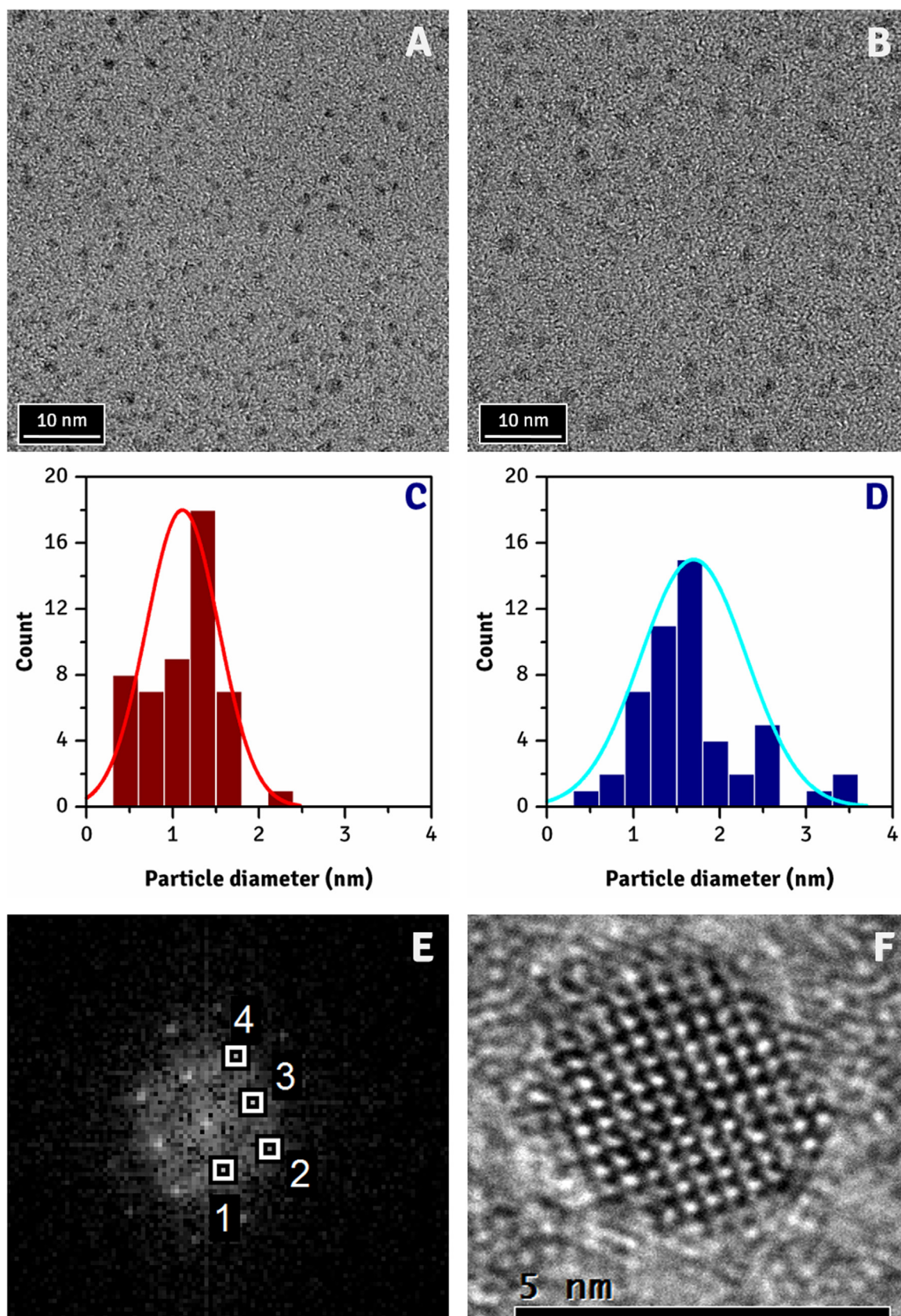
Fig. 2. Micrograph analysis results of the samples: (A) TEM image of Pt nanoparticles, (B) TEM image of Pt_3Sn nanoparticles, (C) corresponding particle size distribution of Pt nanoparticles, (D) corresponding particle size distribution of Pt_3Sn nanoparticles, (E) Fast-Fourier Transformed image of a single Pt_3Sn particle; (F) corresponding original image of the investigated Pt_3Sn particle.
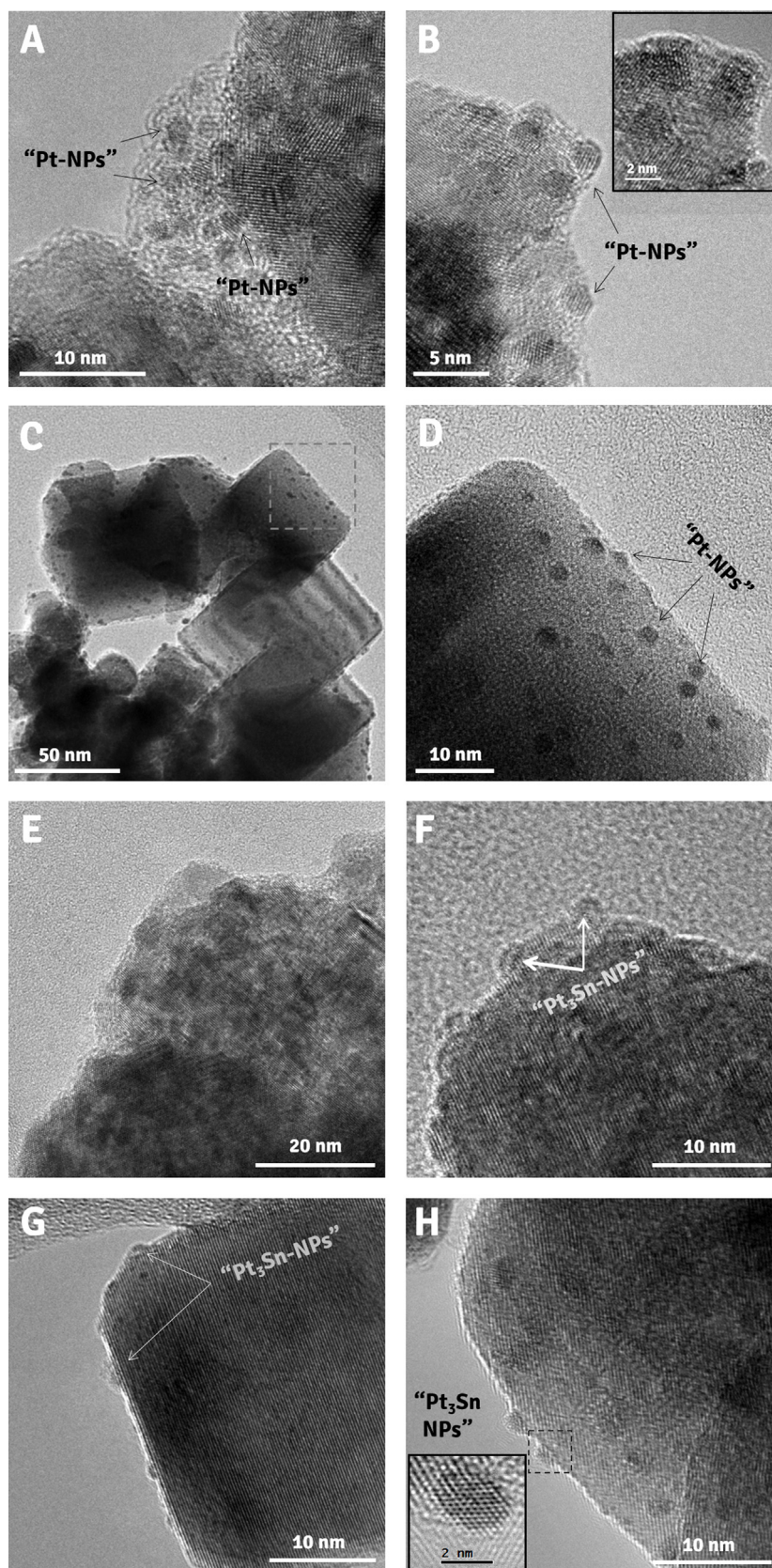
Fig. 3. TEM images of the impregnated samples: (A-B) Pt/CeO$_2$-SCS, (C-D) Pt/CeO$_2$-NC, (E-F) Pt$_3$Sn/CeO$_2$-SCS and (G-H) Pt$_3$Sn/CeO$_2$-NC.

on its Fast Fourier-transformed image (not reported for the sake of brevity) has demonstrated values of d_{spacing} very close to those of theoretical Pt$_3$Sn.

X-ray photoelectron spectroscopy was performed to identify the oxidation states of O, Ce and Pt. Fig. 4A shows four Ce 3d XP spectra of the impregnated samples. Spectrum deconvolution fol-
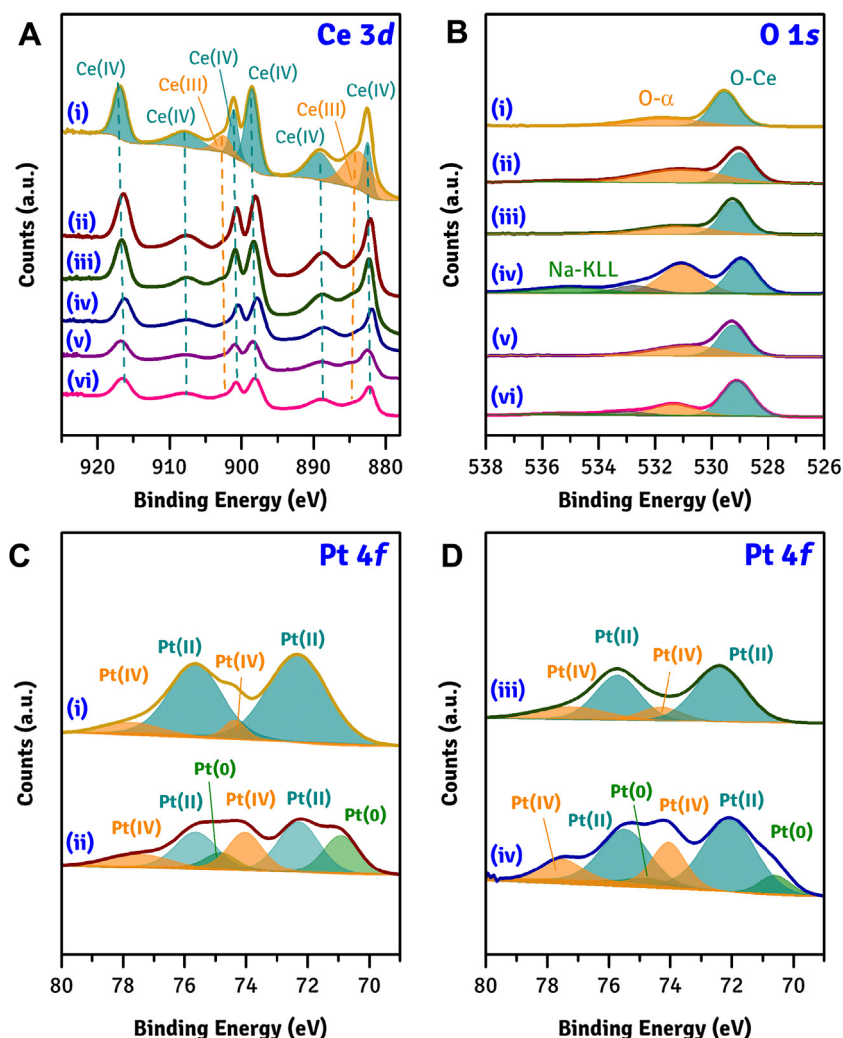
Fig. 4. Deconvoluted X-ray photoelectron spectra of (i) Pt/CeO$_2$-SCS, (ii) Pt/CeO$_2$-NC, (iii) Pt$_3$Sn/CeO$_2$-SCS, (iv) Pt$_3$Sn/CeO$_2$-NC, (v) CeO$_2$-SCS, and (vi) CeO$_2$-NC on different core levels: (A) Ce 3d, (B) O 1s and (C-D) Pt 4f core levels. (For interpretation of the references to color in the text, the reader is referred to the web version of this article.)

Table 4
Total reduced cerium specie (Ce^{3+}) atomic percentages in the prepared samples.

Sample	Ce^{3+} percentage (%)
Pt/CeO$_2$-SCS	28
Pt/CeO$_2$-NC	21
Pt$_3$Sn/CeO$_2$-SCS	32
Pt$_3$Sn/CeO$_2$-NC	23
CeO$_2$-SCS	29
CeO$_2$-NC	21

lowing several literatures [46–48] results in eight different areas: two of which are ascribed to the reduced cerium species [Ce(III)], while others refer to Ce(IV) species. Table 3 reports peak positions (in terms of Binding Energy [BE]) and relative abundances of the identified cerium species. In the 3$d_{5/2}$ region, the first Ce(III) peak appears strongly between 882.8–883.7 eV while in the 3$d_{3/2}$ region, the second Ce(III) peak emerges weakly between 901.7–902.5 eV. The relative quantity of Ce(III) species is summarized on Table 4. From the table, it is evident that the abundance of Ce(IV) species is higher than that of Ce(III) species, indicating the predominant CeO$_2$ phase in the prepared samples. It is instantly noticeable that the atomic percentage of Ce^{3+} is relatively higher in SCS-based samples than that in nanostructured ones (Ce-NC supports). As frequently discussed in previous research [16,17], the preference of solution combustion synthesis for a more reduced ceria environment is due

to the application of high temperature (>600 °C) that prompts the formation of Ce$_2$O$_3$. Impregnation of platinum and platinum-tin alloy does not seem to change significantly the amount of reduced cerium cation (Ce^{3+}), as the percentages of pure ceria samples are somewhat similar to the impregnated counterparts.

Fig. 4B shows the O 1s XP spectra of the impregnated samples. Two peaks are generally observed for ceria-based samples according to several literatures [16–18,49,50]; (1) the O—Ce peak or also known as "O-β", which is assigned at lower BE range (528.8–529.5 eV) and reflects the primary bond of O—Ce in the crystal bulk phase; and (2) the "O-α" peak, which is assigned at higher BE range and signifies the presence of weakly attached oxygenated compounds on the surface level. Table 5 summarizes the relative abundances of the two oxygen species in the samples along with their atomic ratio. Before impregnation with Pt, CeO$_2$-SCS has higher surface oxygen concentration than CeO$_2$-NC, most likely taking form as hydroxyls (OH$^-$) or carbonates as the species generally appears between 530.6–531.1 eV [51]. On the other hand, the O-α peak position of CeO$_2$-NC is observed at 531.3 eV; the value associated to the appearance of O$^-$ ions [51]. This species has a smaller O-atom coordination number than the regular sites' and a higher covalence of the metal – O bonds. After the impregnation with Pt, chemical shifts to higher BE (531.2 and 531.7 eV for Pt and Pt$_3$Sn/CeO$_2$-SCS respectively) are seen in the case of SCS-based catalyst. The quantity of O-α also decreases upon the impregnation

Table 5
Relative abundances of oxygen species derived from the deconvolution of O 1s XP spectra.

Sample	O-α		O—Ce		O-α/O—Ce
	BE (eV)	%-atom	BE (eV)	%-atom	
Pt/CeO$_2$-SCS	531.7	38	529.5	62	0.61
Pt/CeO$_2$-NC	531.1	57	529.0	43	1.33
Pt$_3$Sn/CeO$_2$-SCS	531.2	41	529.2	59	0.69
Pt$_3$Sn/CeO$_2$-NC	531.0	56	528.9	44	1.27
CeO$_2$-SCS	530.8	46	529.2	54	0.85
CeO$_2$-NC	531.3	30	529.1	70	0.43

Table 6
Relative abundances of platinum species derived from the deconvolution of Pt 4f XP spectra.

Sample	Pt 4f$_{7/2}$					
	Pt(0)		Pt(II)		Pt(IV)	
	BE (eV)	%-atom	BE (eV)	%-atom	BE (eV)	%-atom
Pt/CeO$_2$-SCS	–	–	72.3	53	74.4	3.9
Pt/CeO$_2$-NC	70.9	18	72.3	28	74.0	17
Pt$_3$Sn/CeO$_2$-SCS	–	–	72.4	45	74.3	9.2
Pt$_3$Sn/CeO$_2$-NC	70.6	6.6	72.1	40	74.1	15

Sample	Pt 4f$_{5/2}$					
	Pt(0)		Pt(II)		Pt(IV)	
	BE (eV)	%-atom	BE (eV)	%-atom	BE (eV)	%-atom
Pt/CeO$_2$-SCS	–	–	75.6	37	77.8	6.56
Pt/CeO$_2$-NC	74.8	7.0	75.6	20	77.5	11
Pt$_3$Sn/CeO$_2$-SCS	–	–	75.7	32	77.2	14
Pt$_3$Sn/CeO$_2$-NC	74.7	2.7	75.5	27	77.5	8.8

Sample	Total percentage of each species (%-atom)		
	Pt(0)	Pt(II)	Pt(IV)
Pt/CeO$_2$-SCS	–	89	11
Pt/CeO$_2$-NC	25	47	28
Pt$_3$Sn/CeO$_2$-SCS	–	77	23
Pt$_3$Sn/CeO$_2$-NC	9	67	24

Table 7
Specific rates of CO and NO oxidations of the prepared samples.

Sample	Specific rate of CO oxidation[a] (10^2 mmol$_{CO}$ h^{-1} m^{-2})	Specific rate of NO oxidation[b] (10^2 mmol$_{NO}$ h^{-1} m^{-2})
Pt/CeO$_2$-SCS	13.9	3.81
Pt/CeO$_2$-NC	6.13	11.7
Pt$_3$Sn/CeO$_2$-SCS	3.00	1.62
Pt$_3$Sn/CeO$_2$-NC	4.36	4.61
CeO$_2$-SCS	0.00	1.34
CeO$_2$-NC	0.00	4.10

[a] Calculated at 50 °C.
[b] Calculated at 300 °C.

with platinum. On the other hand, the CeO$_2$-NC samples become richer in surface oxygens post-impregnation. Chemical shifts to lower BE are observed, but rather scarce. In the spectra of Pt/CeO$_2$-NC and Pt$_3$Sn/CeO$_2$-NC, a broad peak of Na-KLL Auger transition is observed at about 535 eV [52], most likely originating from the unwashed sodium salt.

The deconvoluted Pt 4f spectra are shown on Fig. 4C and D of Pt- and Pt$_3$Sn-impregnated samples, respectively. Table 6 summarizes the relative abundances of platinum species with their corresponding peak positions. Spectrum deconvolution of all samples, based on several references reported elsewhere [53–56], shows that the dominant oxidation state of the deposited Pt nanoparticles is 2+ [Pt(II)], marked in the figure by the light blue area (peak appearance between 72.1–72.4 eV in the 4f$_{7/2}$ region and between 75.5–75.7 eV in the 4f$_{5/2}$). This comes as no surprise since the normal calcination process oxidizes the zerovalent Pt [Pt(0)] into Pt(II). Pt species, that possibly interacts with the ceria support, also exists in the sample

and is marked in the figure by the orange area (peak appearance between 74.0–74.4 in the 4f$_{7/2}$ region and between 77.2–77.8 eV 4f$_{5/2}$ region). Surprisingly, some zerovalent Pt ("green areas" at the second spectrum on each subfigure) remains only in the nanocubic samples even after calcination. The presence of Pt(0) is identified as small peaks between 70.6–70.9 eV 4 in the 4f$_{7/2}$ region and between 74.7–74.8 eV in the 4f$_{5/2}$ region. Table 6 totals the quantity of platinum species in each sample. Pt(II) specie is present at around 70–90 percent of the total Pt impregnated on CeO$_2$-SCS samples and at 40–70 percent on CeO$_2$-NC samples. In addition, Pt(0) species exists at a relatively small amount (around 9–30 percent) on CeO$_2$-NC samples. The CeO$_2$-SCS samples contain predominantly Pt(II) species, but very few Pt(IV). On the other hand, Pt(IV) species can be found in a considerable amount in the CeO$_2$-NC samples. The presence of Sn, as seen on Table 6, increases the proportion of oxidized Pt species. In the case of CeO$_2$-SCS, the relative quantity of Pt(IV) species increases nearly three-fold. In the case of CeO$_2$-NC,
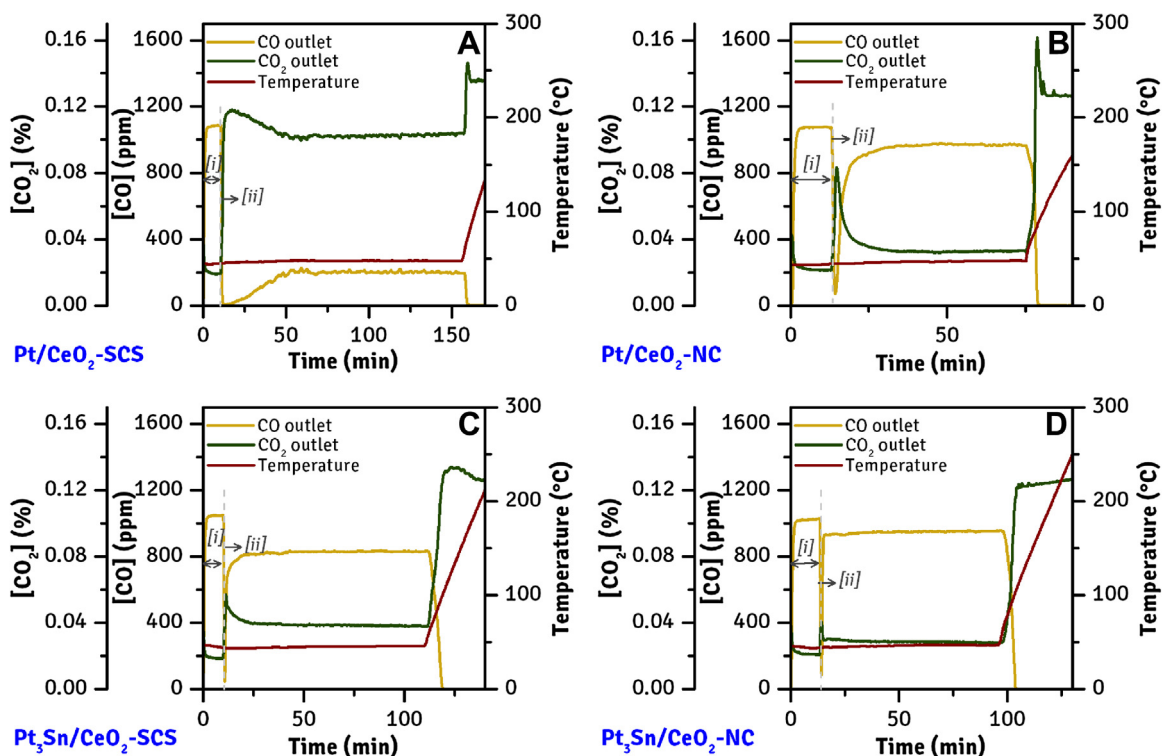
Fig. 5. Transient profiles of CO oxidation catalytic tests over (A) Pt/CeO₂-SCS, (B) Pt/CeO2-NC, (C) Pt₃Sn/CeO₂-SCS and (D) Pt₃Sn/CeO₂-SCS catalysts.
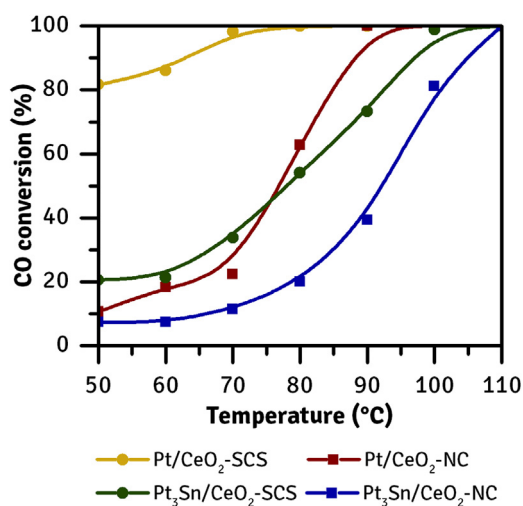

Fig. 6. CO conversion as a function of temperature after the isothermal step at 50 °C. (For interpretation of the references to color in the text, the reader is referred to the web version of this article.)

the presence of Sn suppresses the quantity of zerovalent Pt and shifts the oxidation state to Pt(II) and Pt(IV).

3.2. Catalytic activities

3.2.1. CO oxidation

The transient profiles of CO_x outlet concentrations and temperature during the CO oxidation catalytic activity tests with four impregnated samples are shown on Fig. 5. Table 7 summarizes specific rates of the reaction of the prepared samples at 50 °C. CeO₂-SCS and CeO₂-NC are inactive at this temperature towards CO oxidation, hence zero rates [57]. Pt/CeO₂-SCS (Fig. 6A) has the most remarkable activity among the prepared samples, as at 50 °C the

concentration of CO (yellow curve) falls instantly from 1000 ppm to zero and saturates at about 180 ppm (≈82% CO conversion). After the ramp is activated, CO concentration declines rapidly and 100% conversion is reached at about 80 °C. A small peak of CO_2 is formed at the beginning of 100% conversion, marking the initial stage of CO_2 desorption from the catalyst, followed by a progressive return of the concentration to its theoretical value (close to 1000 ppm). Similar trends are also encountered in the case of Pt/CeO₂-NC, however its activity is much lower than its SCS counterpart. Soon after the flow is switched from bypass to main reactor, the concentration of CO falls to zero but saturates quickly at about 990 ppm (≈10% CO conversion), very close to the fed CO concentration. The huge disparity in low-temperature catalytic activity between Pt/CeO₂-SCS and Pt/CeO₂-NC may root in several possible causes: (1) the specific surface area, that is five times higher in CeO₂-SCS than that in CeO₂-NC; (2) the richer Pt−O phases in the Pt/CeO₂-SCS sample than in the Pt/CeO₂-NC, that tendentiously gives rise to a direct Mars-van Krevelen (M-vK) reaction mechanism, in which the oxide surfaces facilitate extraction of oxygen atoms by CO, after which the oxygen vacancies are replenished with oxygen from the gas bulk phase [58–60]. The reaction involving zerovalent Pt metal on the surface of CeO₂-NC might initially invoke CO adsorption on Pt sites via Langmuir-Hinshelwood (L-H) mechanism, then CO spillover to the ceria support and finally CO oxidation on the surface of ceria with surface and lattice oxygen via M-vK mechanism.

A sharper post-isotherm CO_2 desorption peak is noticed in the test with Pt/CeO₂-NC, indicating more intense CO adsorption in this sample most probably due to the presence of Pt(0) species. The CO_2 desorption process encountered in the tests with both Pt-impregnated samples can be explained as follows: CO adsorbs fast and strongly onto Pt while the reaction between adsorbed CO and O tends to occur more slowly, most likely due to the competition between CO and O in occupying the same Pt site [61]. CO_2 desorption step, according to Nijhuis et al. [62], may be slower than the reaction on the surface despite the weak CO_2 attachment to Pt. Therefore, at above 100 °C the reaction becomes sufficiently fast
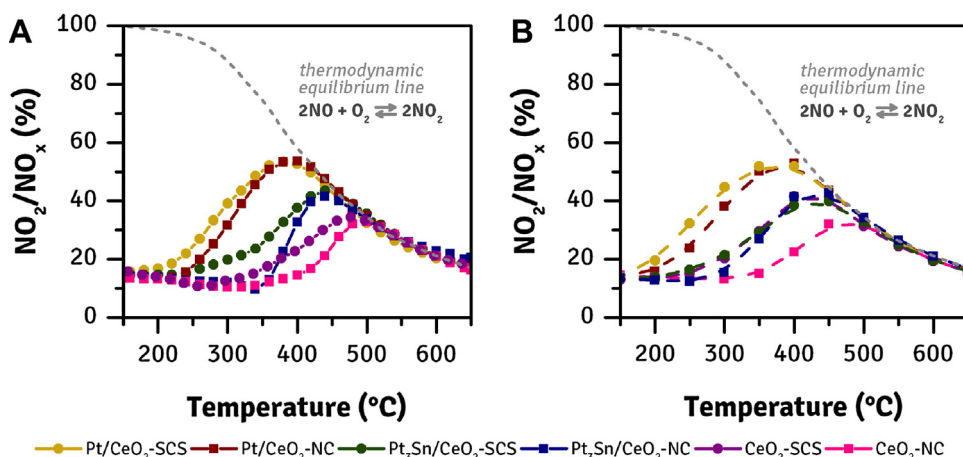
Fig. 7. NO_2 percentage in NO_x mixture as a function of temperature during NO oxidation catalytic tests in (A) ramping and (B) stepwise isothermal modes. (For interpretation of the references to color in the text, the reader is referred to the web version of this article.)

while CO_2 destabilizes slowly and initially accumulates at a large amount forming a peak. The slow comeback of CO_2 to its balanced value (1000 ppm) proceeds afterwards, such a speed is likely due to low gas volumetric flow rate. Fig. 6 shows CO conversion, as a function of temperature, of the impregnated samples during the ramp, carried out right after the saturation at 50 °C. Pt/CeO_2-SCS has undisputedly the most superior intrinsic activity in the series and this is confirmed through its specific reaction rate on Table 7. The specific rate of Pt/CeO_2-NC is about 0.4 times lower than that of Pt/CeO_2-SCS. Despite being very inactive at low temperature, Pt/CeO_2-NC responds quickly towards the reaction after 70 °C and attains the total CO conversion at 90 °C (10 °C higher than that of Pt/CeO_2-SCS).

The Pt_3Sn-impregnated samples, as expected, exhibit lower activity towards CO oxidation compared to the Pt-impregnated ones since the quantity of Pt is reduced. At 50 °C, the CO conversion is around 21% for Pt_3Sn/CeO_2-SCS and 7% for Pt_3Sn/CeO_2-NC. From Table 7, it is also known that specific rates of reaction of the Pt_3Sn-impregnated catalysts are generally lower than the Pt-impregnated ones. It has been investigated elsewhere via an *in-situ* IR CO monitoring that CO adsorption onto a Pt-Sn generally results in lower CO stretching band intensity than that onto a pure Pt [63], thus suggesting a weaker adsorption on Pt-Sn. Interestingly, Pt_3Sn/CeO_2-NC is intrinsically more active than Pt_3Sn/CeO_2-SCS towards CO oxidation (4.36×10^2 and 3.00×10^2 $mmol_{CO}$ h^{-1} m^{-2} for Pt_3Sn/CeO_2-NC and Pt_3Sn/CeO_2-SCS, respectively) despite the low surface area. At higher temperature the activity of Pt_3Sn/CeO_2-NC resumes (observed on Fig. 6 from the sharp increase between 80 and 100 °C) most likely due to the reactive structures, while the activity slowly augments in the case of Pt_3Sn/CeO_2-SCS; the same comportment observed previously in the Pt-impregnated samples.

3.2.2. NO oxidation

The tests with NO oxidation aim at investigating the catalytic activity of small Pt and Pt_3Sn nanoparticles towards maximum NO_2 production at low temperature. Fig. 7 shows profiles of NO_2 molar percentage in the NO_x mixture (NO and NO_2) as a function of temperature obtained from the tests in ramping (Fig. 7A) and isothermal modes (Fig. 7B). In general, the outcome of the test appears as an asymmetric bell curve, the first half of which with an ascending trend represents the kinetically-controlled regime, while the descending part signifies a reaction limitation due to thermodynamics. The peak, thus, indicates maximum NO_2 obtainable during the reaction. The dashed line crossing the main curves represents the thermodynamic equilibrium of NO oxidation. The results of the tests in ramping mode with bare ceria (violet curve for CeO_2-

SCS and pink curve for CeO_2-NC in Fig. 7A) show that the production of NO_2 is rather low (NO_2 molar percentage in mixture = 34% for CeO_2-SCS and 32% for CeO_2-NC). The reaction mediated with CeO_2-NC occurs efficiently in a narrow temperature window, ranging from approximately 450–550 °C, while with CeO_2-SCS it runs at lower and wider temperature window (350–550 °C). The results of the tests involving isothermal steps as seen on Fig. 7B demonstrates a similarity in activity trend to the ones with ramping mode. The use of isothermal steps in the catalytic test aims at allowing the reaction to approach as closely as possible to its equilibrium at a constant temperature, giving eventually more representative results in terms of catalytic activity. The trend similarity between the tests with ramping mode and isothermal steps suggests that the use of 5 °C min^{-1} as the programmed ramp is sufficiently safe for maintaining reliable data. Table 7 summarizes the specific rate of NO oxidation of the prepared samples at 300 °C, calculated using the data from tests with isothermal steps. The specific rate of CeO_2-NC is about three times higher than that of CeO_2-SCS (4.10×10^2 and 1.34×10^2 $mmol_{NO}$ h^{-1} m^{-2} for CeO_2-NC and CeO_2-SCS, respectively). This means that at relatively low temperature CeO_2-NC is intrinsically more active than CeO_2-SCS towards NO oxidation despite the low surface area. This finding gives a new insight into structure sensitivity of NO oxidation on ceria, to which little attention has been paid.

The presence of Pt not only boosts the production of NO_2 but also shifts the temperature window to a lower range. Both Pt/CeO_2-SCS and Pt/CeO_2-NC (represented by yellow and red curves, respectively) exhibit similar performance towards NO oxidation, achieving about 53% NO conversion into NO_2 at 400 °C. The two samples only differ in light-off temperature, which is slightly lower for Pt/CeO_2-SCS. Previous investigation has concluded the propensity of NO oxidation on Pt-based catalysts to conform L-H mechanism [64], in which the reaction begins with the chemisorption of reactants NO and O_2, preferably on the Pt coordinatively unsaturated sites, and then continues with dissociation of adsorbed molecular O_2 into two O adatoms. The reaction between NO and O adatom occurs at the surface via a formation of O—N—O complexes and finally finishes with NO_2 desorption from the surface [65]. It has also been demonstrated via theoretical studies that the adsorption of NO and O on PtO_2(110) is rather weak compared to that on Pt(111), leading to a high barrier for O_2 dissociation [65]. This may explain the early reaction in Pt/CeO_2-SCS as it lacks Pt(IV) species. However, the intrinsic activity remains higher in Pt/CeO_2-NC than in Pt/CeO_2-SCS, as the specific rate of the nanocubic sample is three times higher than that of the SCS sample (see Table 7).

Table 8
Results from soot oxidation catalytic tests in the absence and the presence of NO_x.

Sample	$T_{10\%}$ (°C)	$T_{50\%}$ (°C)	$T_{90\%}$ (°C)	Specific rate ($mmol_{soot} \, g_{cat}^{-1} \, h^{-1}$)[a]
In the absence of NO (10%-v O_2 in N_2)				
Pt/CeO_2-SCS	511	595	636	0.125
Pt/CeO_2-NC	500	571	619	0.171
Pt_3Sn/CeO_2-SCS	506	586	631	0.167
Pt_3Sn/CeO_2-NC	482	556	614	0.292
CeO_2-SCS	502	591	635	0.156
CeO_2-NC	492	580	637	0.184
In the presence of NO (550 ppm NO + 10%-v O_2 in N_2)				
Pt/CeO_2-SCS	414	501	555	0.998
Pt/CeO_2-NC	406	484	552	1.544
Pt_3Sn/CeO_2-SCS	445	529	583	0.576
Pt_3Sn/CeO_2-NC	423	498	555	1.445
CeO_2-SCS	453	544	596	0.410
CeO_2-NC	446	531	580	0.759

[a] Calculated at 450 °C.

Table 9
Relative abundances of platinum species in the aged Pt/CeO_2 samples derived from the deconvolution of Pt $4f$ XP spectra.

Sample	Pt $4f_{7/2}$					
	Pt(0)		Pt(II)		Pt(IV)	
	BE (eV)	%-atom	BE (eV)	%-atom	BE (eV)	%-atom
Pt/CeO_2-SCS	70.9	11	72.7	29	74.3	33
Pt/CeO_2-NC	70.7	23	72.1	33	73.9	18

Sample	Pt $4f_{5/2}$					
	Pt(0)		Pt(II)		Pt(IV)	
	BE (eV)	%-atom	BE (eV)	%-atom	BE (eV)	%-atom
Pt/CeO_2-SCS	–	–	76.2	24	78.7	3
Pt/CeO_2-NC	74.7	7	75.5	7.5	76.8	12

Sample	Total percentage of each species (%-atom)		
	Pt(0)	Pt(II)	Pt(IV)
Pt/CeO_2-SCS	11	53	36
Pt/CeO_2-NC	29	41	30

The two Pt_3Sn-impregnated samples (represented by green and blue curves for SCS and NC samples, respectively) shows moderate NO_2 productions (41–43% of NO_2 in NO_x), which are evidently higher than those in the case of bare ceria samples and lower than those in the case of Pt-impregnated samples. This is also confirmed via specific reaction rates, which are slightly higher from those of bare ceria, but much lower from those of Pt-containing samples. The presence of Sn, despite its main objective is to reduce the quantity of Pt, may influence the adsorption of NO on the surface and further the production of NO_2. Investigation by Xu and Koel on Sn/Pt(111) surface alloy has shown that the presence of Sn strongly reduces NO adsorption onto the substrate as it modifies the electronic properties that reduce the ability of the substrate to bond covalently with an unpaired electron of NO in $2\pi^*$ orbital [66].

3.2.3. Soot oxidation

Fig. 8 shows the results of the catalytic activity tests with soot oxidation. The graphs in the first column (Fig. 8A, C and E) represent the results obtained from the tests in the absence of NO while others in the second column (Fig. 8B, D and F) summarize the results obtained from the tests in the presence of NO. In this subsection, only the graphs in the first column are taken into account in the discussion. The reaction of soot with oxygen can be expressed in general fashion as follows:

$$C + (1 - 0.5\alpha)O_2 \leftrightarrow \alpha CO + (1 - \alpha)CO_2 \quad (1)$$

while α symbolizes the stoichiometric coefficient of CO in the reaction. Therefore, three profiles are normally obtained from the tests: soot conversion, CO_2 concentration and CO concentration as functions of temperature. Table 8 summarizes the data of the temperatures at which 10%, 50% and 90% soot conversions are reached, extracted from soot conversion curves. The table also shows specific reaction rates (in $mmol \, C \, g^{-1} \, h^{-1}$) of all samples at 450 °C; the temperature at which reaction is still kinetically-controlled.

Pure ceria samples were tested and their results are used for references. The results show that CeO_2-SCS (violet curve) has lower activity than CeO_2-NC (pink curve) as the curve of the former stretches in the higher temperature range ($T_{50\%}$ are 591 °C and 580 °C for CeO_2-SCS and CeO_2-NC, respectively). The specific reaction rate of CeO_2-NC also appears higher than that of CeO_2-SCS. This trend confirms previous findings and recalls the importance of catalyst's physical structure in improving intrinsic activity towards soot oxidation [16–18]. CO_2 production appears to be higher in the reaction mediated with CeO_2-SCS, while CO production is evidently higher in the case of CeO_2-NC. The employment of Pt/CeO_2-SCS (yellow curve) surprisingly shows no improvement from the initial oxidation activity with CeO_2-SCS. On the other hand, Pt/CeO_2-NC (red curve) renders soot oxidation slightly more active compared to its bare ceria counterpart ($T_{50\%}$ for Pt/CeO_2-NC is 571 °C), although the specific reaction rates of Pt-containing samples are slightly lower than those of bare ceria. These findings imply a minor contribution of Pt to the improvement of soot oxidation, in contrast to the previous tests with CO and NO oxidations. Bueno-López et al.
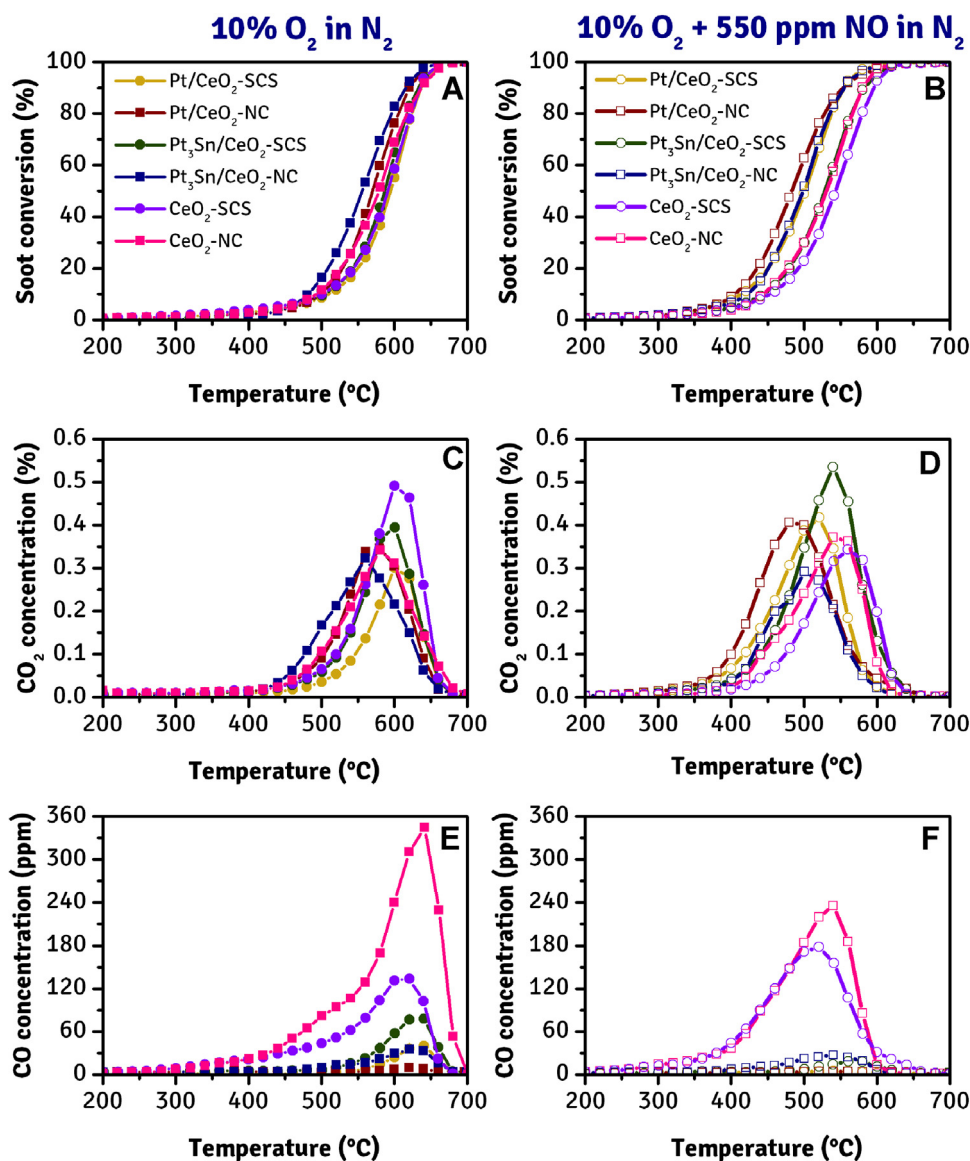
Fig. 8. Soot conversion, CO_2 and CO concentrations as functions of temperature during soot oxidation catalytic tests in the absence of NO_x (A, C and E) and in the presence of NO_x (B, D and F). (For interpretation of the references to color in the text, the reader is referred to the web version of this article.)

suggested that soot oxidation mediated with Pt/CeO_2 occurs following these three steps: (1) dissociative adsorption of dioxygen on two Pt adjacent sites; (2) oxygen transfer from Pt sites to the surface of ceria, or more commonly known as "oxygen spillover"; and (3) contact between soot and the so-called "active oxygen species" liberated from the surface/lattice of ceria [67]. In this mechanism, Pt only takes part in capturing and transferring oxygen from bulk phase to the surface of ceria. Therefore, the problem of seemingly inactive Pt in Pt/CeO_2-SCS may root in either the low rate of O_2 adsorption onto Pt or the low rate of oxygen spillover to the surface of the support. Low oxygen affinity may occur due to the abundant presence of Pt species of higher oxidation states in Pt/CeO_2-SCS. It creates high barriers for O_2 dissociative adsorption to occur on Pt surfaces. If oxygen adsorption or oxygen spillover is limited, then the oxygen necessary for the reaction is solely supplied by ceria. This eventually explains the identical catalytic activities between CeO_2-SCS and Pt/CeO_2-SCS. On the other hand, Pt/CeO_2-NC benefits from the Pt(0) species that enables better adsorption and transfer of oxygen from bulk phase to the ceria surface. Therefore, the catalytic activity is higher than its SCS counterpart. Regarding the CO_x con-

centrations, both Pt/CeO_2-SCS and Pt/CeO_2-NC are able to suppress the formation of CO, as observed in Fig. 8E.

Unexpectedly, the presence of Sn increases catalytic activity towards soot oxidation. On Fig. 8A, Pt_3Sn/CeO_2-SCS (green curve) appears to be more active than Pt/CeO_2-SCS and CeO_2-SCS albeit insignificantly, while Pt_3Sn/CeO_2-NC (blue curve) is the most active catalyst among the samples. Interestingly, the specific rates of these samples are the highest in the series. The presence of Sn possibly inhibits CO poisoning on Pt as is previously confirmed during the tests with CO oxidation (see Section 3.2.1). Less adsorbed CO on Pt therefore translates as more unmasked Pt sites accessible by bulk oxygen. Balakrishnan and Schwank have also demonstrated that the amount of chemisorbed oxygen on bimetallic Pt–Sn catalysts increases with the increasing Sn content [68], thus indicating the better oxygen affinity to Sn than to Pt. In contrast, the amount of chemisorbed CO on Pt–Sn catalysts decreases with the increasing Sn content [68], corroborating the aforementioned possibility of Sn as CO poisoning inhibitor. Another possible reason for the high catalytic activity of Pt–Sn catalyst is the fact that SnO_x has a similar redox property to ceria; it enables oxygen intake-uptake on the
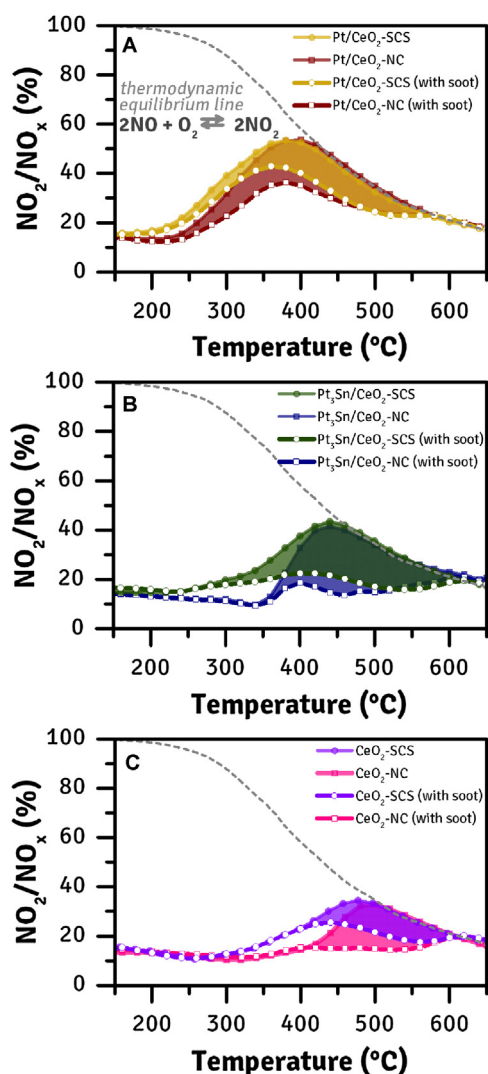
Fig. 9. NO_2 percentage in NO_x mixture as a function of temperature during NO_x-assisted soot oxidation catalytic tests over (A) Pt-impregnated, (B) Pt_3Sn-impregnated and (C) Pt-free ceria catalysts.
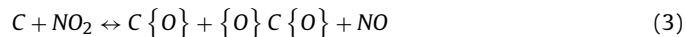
surface, from which reactions governed by M-vK mechanism can benefit. This property could also be advantageous in soot oxidation as it may enhance the oxygen mobility and diffusion to the ceria support.

3.2.4. NO_x-assisted soot oxidation

Soot oxidation catalytic tests in the presence of NO_x essentially combine the three former reactions. The mechanism commences with the conversion of NO into NO_2 on the surface of Pt, following this overall reaction:

$$2NO + O_2 \overset{Pt}{\leftrightarrow} 2NO_2 \qquad (2)$$

NO_2, being stronger oxidant than O_2, actively attacks soot on the surface, initially forming carbon-oxygen compounds called "surface-oxygenated carbon" complexes (SOCs) [69], 3represented in Equation (3) as $C\{O\}$ and $\{O\}C\{O\}$. The former representation refers to the unstable SOCs as the number of oxygen increases on the surface.

$$C + NO_2 \leftrightarrow C\{O\} + \{O\}C\{O\} + NO \qquad (3)$$

The oxygenation of soot could also occur with O_2 but at relatively high temperature. NO_2 not only attacks soot but also the ceria support. Setiabudi et al. discovered in a DRIFT study that

NO_2 oxygenates ceria by donating its oxygen to replenish the O-vacancies via O—N—O complex intermediates, e.g. mono- or bidentate nitrates, chelating-nitros and bridging nitrites [70]. The SOCs decompose further with or without reactions with oxidants (both NO_2 and O_2), forming CO, CO_2 and NO. It is also known that NO_2 participation in soot oxidation depends on soot-catalyst contact; in tight contact its participation is limited [71].

The NO_x concentration profile during the test is summarized on Fig. 9, as a plot of NO_2 percentage in NO_x as a function of temperature. In general, the peak of NO_2 percentage decreases in the presence of soot due to reactions between the two compounds. The area between the plot obtained from the tests with NO oxidation and the one obtained from the tests with soot oxidation in the presence of NO (discerned on the legend as "with soot") simply reflects the disappearance of NO_2 due to reactions. Light-off temperatures in both tests are always lower for the SCS samples than those for the nanostructured ones, implying the role of surface area. Fig. 9A shows the plots derived from the tests with Pt/CeO_2-SCS (yellow curves/areas) and Pt/CeO_2-NC (red curves/areas). The disappearance of NO_2 starts at early 250 °C in both cases, suggesting the early consumption of NO_2 for soot oxygenation since CO_2 signal is not yet observed (see the corresponding Fig. 8D). As the temperature increases, the consumption of NO_2 intensifies, creating differences in integral areas between two tests. The area appears to be higher for Pt/CeO_2-NC, with which more intense NO_2 consumption is suggested to occur in the reaction. This corroborates the soot conversion trends shown previously on Fig. 8B, on which the range of conversion is lower for Pt/CeO_2-NC than that for Pt/CeO_2-SCS (On Table 8, $T_{50\%}$ are 484 °C and 501 °C for Pt/CeO_2-NC and Pt/CeO_2-SCS, respectively). The specific reaction rate of Pt/CeO_2-NC is also much higher than that of Pt/CeO_2-SCS (0.49 and 0.33 mmol C g^{-1} h^{-1} for Pt/CeO_2-NC and Pt/CeO_2-SCS, respectively), meaning that Pt/CeO_2-NC is intrinsically active towards NO_x-assisted soot oxidation at low temperatures. The highest catalytic activity of Pt/CeO_2-NC suggests the importance of tailoring catalyst's physical dimension. Small Pt nanoparticles, irrespective of their oxidation states, always favor high catalytic activity as it provides more surface area for reactions and adsorptions to occur. Well-defined ceria nanocubes, on the other hand, grant enhanced catalytic activity towards soot oxidation thanks to their reactive planes and improved electronic properties. Together, these two catalytic components form a synergy, enabling the production of NO_2 at low temperature whilst maintain at the same time the cooperative contact between soot and catalyst.

In the previous discussion, the use of Sn as the alloying agent for Pt reduces the activity towards NO oxidation but unexpectedly increases the activity towards soot oxidation. In the tests with NO_x-assisted soot oxidation, however, the performance of Pt_3Sn-impregnated catalysts varies depending on the type of the support. At 400 °C, these catalysts are intrinsically less active than their Pt counterparts, as observed via specific reaction rate data on Table 8 (0.20 and 0.23 for Pt_3Sn/CeO_2-SCS and Pt_3Sn/CeO_2-NC respectively). Above 400 °C, it is observed on Fig. 8B that the activity of Pt_3Sn/CeO_2-SCS (green curve) is much lower than its Pt counterpart (On Table 8, $T_{50\%}$ is 529 °C for Pt_3Sn/CeO_2-SCS), even nearly identical to that of CeO_2-NC (pink curve). The performance of Pt_3Sn/CeO_2-NC (red curve) is surprisingly much more active than its SCS counterpart (On Table 8, $T_{50\%}$ is 498 °C for Pt_3Sn/CeO_2-NC) and even similar to Pt/CeO_2-SCS. With a reduced quantity of Pt, Pt_3Sn/CeO_2-NC manages to approach the activity of the Pt/CeO_2-NC, which is the most active catalyst in the series. This confirms the possibility of Pt–Sn alloy as an alternative to pure Pt. Fig. 9B shows that the NO_2 consumption during the reaction with Pt_3Sn-impregnated catalysts, represented by green (Pt_3Sn/CeO_2-SCS) and blue areas (Pt_3Sn/CeO_2-NC), seems to be more intense than the consumption during the reaction with Pt-impregnated catalysts,
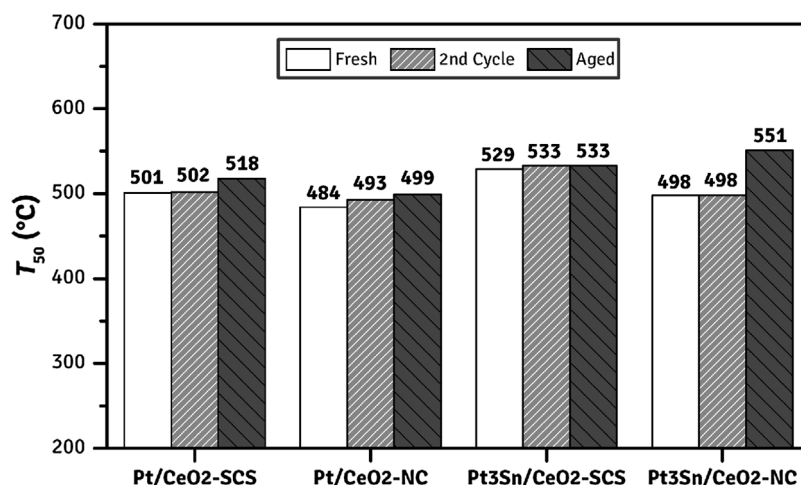
Fig. 10. Results of stability tests in terms of $T_{50\%}$ of the fresh start (white bar), the second cycle (gray bar) with the previously used catalyst, and the test with aged catalysts (dark gray bar).

as the two areas appear larger. This suggests that the mediation with Pt_3Sn-impregnated catalysts may result in a more active participation of NO_2 during high-temperature oxidation reaction.

The interaction between NO_2 and soot on bare ceria supports is observed on Fig. 9C. Despite the absence of Pt as the provider of active sites, NO_2 can actually be produced with the help of ceria and readily react with soot. CeO_2-SCS facilitates early interaction between NO_2 and soot thanks to its high surface area. However, as the temperature rises, the NO_2 consumption is higher with the help of CeO_2-NC. This eventually confirms the significance of morphologically-tailored ceria, even in the case of NO_x-assisted soot oxidation. As expected, the catalytic activity of CeO_2-NC is higher than CeO_2-SCS (see Fig. 8B) despite a small difference in $T_{50\%}$ at about 13 °C.

It is important to notice the decrease of CO production in NO_x-assisted soot oxidation (Fig. 8F). This implies that NO_x interacts equally with CO, possibly via this following reaction:

$$CO + NO_2 \leftrightarrow NO + CO_2 \tag{4}$$

although the increase in CO_2 concentration might hardly be observed on Fig. 8D since CO_2 concentration is about ten times higher than the one of CO.

3.2.5. Catalyst stability

Fig. 10 summarizes the data of T_{50} obtained from the stability tests. In the second cycle (gray bar) where catalysts are already used once in normal tests with NO_x-assisted soot oxidation, the catalytic performances are relatively constant compared to those in the fresh start (white bar) with the T_{50} deviation from the fresh start ranging from 0 to 9°. Despite the reuse, the catalytic activity trend observed in the fresh start (see Section 3.2.4) is still well-preserved; the Pt/CeO_2-NC being the most performing catalyst for the reaction. Interestingly, the performances of the aged catalysts (dark gray bar) vary little from those of fresh and used catalysts. In the Pt catalyst series, the increases of T_{50} are 17 and 15° for Pt/CeO_2-SCS and Pt/CeO_2-NC respectively. This finally foregrounds the importance of silyl ligands as the particle keeper, not only during the synthesis but also during the aging process when the particles are impregnated onto supports. Exposure to air at an elevated temperature during the calcination converts the surrounding silyl ligands into a SiO_2 patch. This silica practically fences in the Pt NP and prevents it from enlarging as well as migrating to neighboring particles. The same effect has equally been encountered in the case of Si-stabilized Ni NP, reported elsewhere [72]. Meanwhile, the activities of Pt_3Sn catalysts after aging treatment seem dependent on the
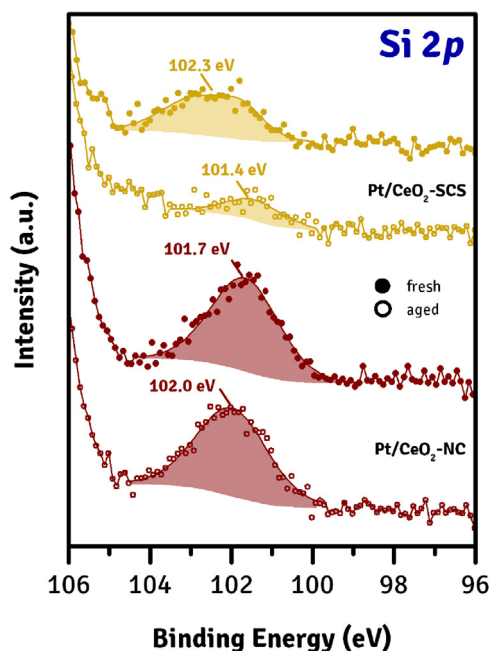

Fig. 11. Deconvoluted X-ray photoelectron spectra of fresh (●) and aged (○) Pt/CeO_2-SCS (yellow) and Pt/CeO_2-NC (red) samples on Si $2p$ core level. (For interpretation of the references to color in this figure legend, the reader is referred to the web version of this article.)

support used. Pt_3Sn/CeO_2-SCS has the lowest T_{50} increase at about 4 °C from the fresh start, while unfortunately Pt_3Sn/CeO_2-NC has the highest T_{50} increase (43 °C) and eventually becomes the least performing catalyst. Unlike Si–Pt bonding, Sn–Pt bonding results in rather an unprotected Pt_3Sn alloy that have no outer control against particle enlargement. Support morphology may give this indirect control as it determines the quality of particle deposition. CeO_2-SCS is microstructured, fairly porous and has plenty of corrugated surfaces; a combination of which might shelter well the particles and inhibit them from migration to form larger clusters. On the other hand, CeO_2-NC is non-porous and, most importantly, dominated by smooth surfaces due to abundant (100) planes. This type of surface provides no topological barriers for unguarded Pt_3Sn NPs to cluster.

In order to better characterize the Si patch, additional XPS analysis has also been carried out with the aged samples. Fig. 11 shows the deconvoluted Si $2p$ XP spectra of fresh and aged Pt/CeO_2-
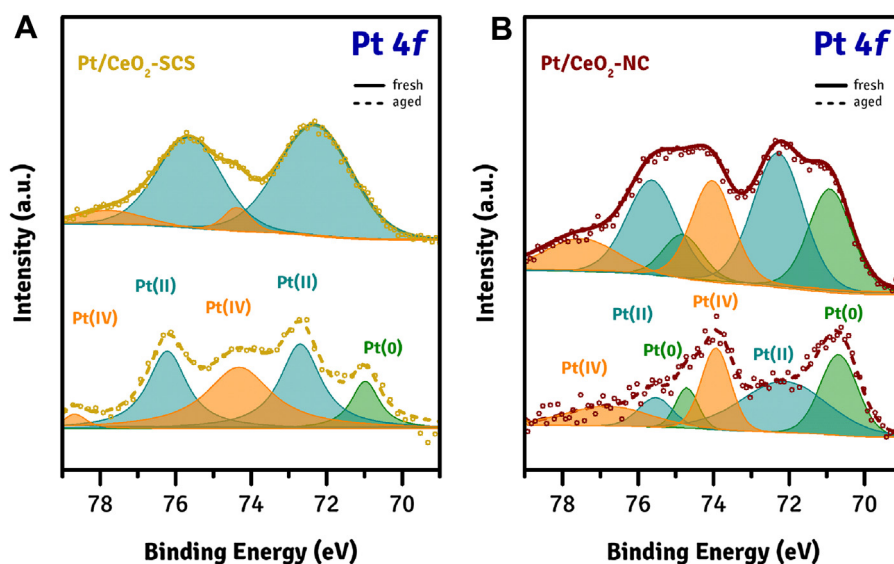
Fig. 12. Deconvoluted X-ray photoelectron spectra of fresh (●,–) and aged (○,–) Pt/CeO$_2$-SCS (A) and Pt/CeO$_2$-NC (B) samples on Pt *4f* core level.

SCS and Pt/CeO$_2$-NC samples. The deconvoluted peaks appear in BE range of 101.4–102.3 eV and can be ascribed as siloxane (−Si−O−Si−) according to literature [73]. We surmise that the silica patch formed during calcination step consists of repeated siloxanes, protecting Pt in the interior possibly via Si−O−Pt bonding. Elemental Si and pure SiO$_2$, normally observed at 99.4 eV and at 103.5 eV respectively, are not observed in fresh and aged samples. This implies that calcination, normal or even prolonged, does not change the protective nature of the patch. It is also observed from the similarity in peaks that after aging the character of the patch, especially in the case of Pt/CeO$_2$-NC, appears constant. The noticeable difference is, however, observed in the aged sample of Pt/CeO$_2$-SCS, in which the peak intensity decreases.

Fig. 12 finally shows the deconvoluted Pt *4f* XP spectra of fresh and aged Pt/CeO$_2$-SCS and Pt/CeO$_2$-NC samples. Table 9 summarizes the relative abundances of the Pt species in the aged Pt/CeO$_2$ samples (revisit Table 6 for the data of the fresh samples for comparison). On Fig. 12A, it is easily noticed that the now-aged Pt/CeO$_2$-SCS sample contains also Pt(0) species while from Table 9 it can be seen that the abundance of Pt(IV) species increases. Similar results have also been encountered in the aged Pt/CeO$_2$-NC sample: the abundances of Pt(0) and Pt(IV) species increase, but much less markedly than in the case of Pt/CeO2-SCS. Therefore, on the one hand, higher-oxidation state Pt species presumably evolve to Pt(0) during the aging in the presence of oxygen at 700 °C, as a consequence of Pt nanoparticles sintering. On the other hand, the relative abundance of Pt(IV) could remain stable due to the strong Pt-ceria support interaction via Pt−O−Ce bond [74].

4. Conclusion

In this work we have demonstrated that small Pt and Pt$_3$Sn nanoparticles, prepared via stabilization with organosilane and supported on morphology-tailored ceria, render enhanced catalyst activity in NO$_x$-assisted soot oxidation. Our Pt nanoparticles exhibit remarkable catalytic activities in CO oxidation, as they can efficiently convert CO at 50 °C. The oxidation activity is also found to be dependent on the morphology of the support as it is constantly higher with high-surface area ceria than in low-surface area ceria nanocubes. The presence of Sn in the alloy Pt$_3$Sn reduces the catalytic activity. In NO oxidation, similar trends are encountered as samples with Pt nanoparticles give higher NO$_2$ production than

their Pt$_3$Sn counterparts. The effect of support's morphology on the catalytic activity in NO oxidation is almost negligible, yet it becomes prominent in soot oxidation. Nanocubic ceria, irrespective of the impregnated metal, always succeeds in initiating lower temperature soot oxidation. In the absence of NO, the effect of Pt and Pt$_3$Sn on the catalytic activity is far less important than the morphology, since soot oxidation has been famously known to be structure-dependent. However, the presence of Sn gives a little advantage in lowering oxidation temperature. Finally, in the presence of NO, the presence of Pt and Pt$_3$Sn nanoparticles boosts the catalytic activity in soot oxidation. Our most performing catalyst, Pt/CeO$_2$-NC (NC stands for "nanocubes"), has showed its remarkable ability to lower the oxidation temperature at about 80 °C, thanks to the synergy of the active metal nanoparticles and ceria nanocubes that constitute of reactive surfaces. Much to our surprise, the catalytic activity with our Pt$_3$Sn/CeO$_2$-NC approaches its pure Pt counterpart with approximately 10 °C of difference. This suggests the potential of the catalyst as an alternative to reducing the employment of precious metal in automotive catalysis. The thermally aged Pt catalysts have demonstrated good resistance to sintering, owing to the formation of a silica patch encircling the particle. The catalytic activities of the aged Pt$_3$Sn catalysts are, nevertheless, dependent heavily on the textural properties of the support.

References

[1] http://eur-lex.europa.eu/legal-content/EN/ALL/?uri=CELEX:32007R0715.
[2] https://www3.epa.gov/pm/health.html.
[3] S. Bensaid, C.J. Caroca, N. Russo, D. Fino, Can. J. Chem. Eng. 89 (2011) 401–407.
[4] S. Bensaid, D.L. Marchisio, N. Russo, D. Fino, Catal. Today 147 (2009) S295–S300.
[5] T. Nakane, M. Ikeda, M. Hori, O. Bailey, L. Mussmann, SAE Technical Paper (2005) (2005-01-1759).
[6] C. Görsmann, Monatshefte für Chemie 136 (2005) 91–105.
[7] A.P. Walker, Top. Catal. 28 (2004) 1–4.

[8] A. Thiruvengadam, M.C. Besch, D.K. Carder, A. Oshinuga, M. Gautam, Environ. Sci. Technol. 46 (2012) 1907–1913.
[9] E. Aneggi, M. Boaro, C. de Leitenburg, G. Dolcetti, A. Trovarelli, J. Alloys Compd. 408–412 (2006) 1096–1102.
[10] A. Trovarelli, Catal. Rev. Sci. Eng. 38 (1994) 439–450.
[11] S. Damyanova, B. Pawelec, K. Arishtirova, M.V. Martinez Huerta, J.L.G. Fierro, Appl. Catal. A 337 (2008) 86–96.
[12] R. Rao, B.G. Mishra, Bull. Catal. Soc. India 2 (2003) 122–134.
[13] W. Zhan, Y. Guo, X. Gong, Y. Guo, Y. Wang, G. Lu, Chin. J. Catal. 35 (2014) 1238–1250.
[14] H.-F. Wang, Y.-L. Guo, G.-Z. Lu, P. Hu, Angew. Chem. Int. Ed. 48 (2009) 8289–8292.
[15] H.-Y. Li, H.-F. Wang, X.-Q. Gong, Y.-L. Guo, Y. Guo, G. Lu, P. Hu, Phys. Rev. B 79 (2009) 193401.
[16] M. Piumetti, S. Bensaid, N. Russo, D. Fino, Appl. Catal. B 165 (2015) 742–751.
[17] T. Andana, M. Piumetti, S. Bensaid, N. Russo, D. Fino, R. Pirone, Appl. Catal. B 197 (2016) 125–137.
[18] M. Piumetti, S. Bensaid, N. Russo, D. Fino, Appl. Catal. B 180 (2016) 271–282.
[19] E. Aneggi, D. Wiater, C. de Leitenburg, J. Llorca, A. Trovarelli, ACS Catal. 4 (2014) 172–181.
[20] N. Guillén-Hurtado, A. García-García, A. Bueno-López, Appl. Catal. B 174 (2015) 60–66.
[21] H.-X. Mai, L.-D. Sun, Y.-W. Zhang, R. Si, W. Feng, H.-P. Zhang, H.-C. Liu, C.-H. Yan, J. Phys. Chem. B 109 (2005) 24380–24385.
[22] S. Yang, L. Gao, J. Am. Chem. Soc. 128 (2006) 9330–9331.
[23] R. Si, M. Flytzani-Stephanopoulos, Angew. Chem. 120 (2008) 2926–2929.
[24] Z. Hu, X. Liu, D. Meng, Y. Guo, Y. Guo, G. Lu, ACS Catal. 6 (2016) 2265–2279.
[25] J.P.A. Neeft, O.P. van Pruissen, M. Makkee, J.A. Moulijn, Appl. Catal. B 12 (1997) 21–31.
[26] J. van Doorn, J. Varloud, P. Mériaudeau, V. Perrichon, M. Chevrier, C. Gauthier, Appl. Catal. B 1 (1992) 117–127.
[27] S. Salomons, M. Votsmeier, R.E. Hayes, A. Drochner, H. Vogel, J. Gieshof, Catal. Today 117 (2006) 491–497.
[28] H.J. Stein, Appl. Catal B 10 (1996) 69–82.
[29] J.G. Nunan, H.J. Robota, M.J. Cohn, S.A. Bradley, J. Catal. 133 (1992) 309–324.
[30] N. Artioli, R. Matarrese, L. Castoldi, L. Lietti, P. Forzatti, Catal. Today 169 (2011) 36–44.
[31] N. Takahashi, H. Shinjoh, T. Iijima, T. Suzuki, K. Yamazaki, K. Yokota, H. Suzuki, N. Miyoshi, S. Matsumoto, T. Tanizawa, T. Tanaka, S. Tateshi, K. Kasahara, Catal. Today 27 (1996) 63–69.
[32] E. McCarthy, J. Zahradnik, G.C. Kuczynski, J.J. Carberry, J. Catal. 39 (1975) 29–35.
[33] G.S. Zafiris, R.J. Gorte, J. Catal. 140 (1993) 418–423.
[34] Y.F. Chu, E. Ruckenstein, J. Catal. 55 (1978) 281–298.
[35] P.J.F. Harris, J. Catal. 97 (1986) 527–542.
[36] R.M.J. Fiedorow, B.S. Chahar, S.E. Wanke, J. Catal. 51 (1978) 193–202.
[37] C.W. Scheeren, G. Machado, J. Dupont, P.F.P. Fichtner, S.R. Texeira, Inorg. Chem. 42 (2003) 4738–4742.
[38] K. Pelzer, M. Haevecker, M. Boualleg, J.-P. Candy, J.-M. Basset, Angew. Chem. Int. Ed. 50 (2011) 5170–5173.
[39] K. Philippot, B. Chaudret, C. R. Chim. 6 (2003) 1019–1034.
[40] M. Boualleg, D. Baudouin, J.-M. Basset, F. Bayard, J.-P. Candy, J.-C. Dumas, L. Veyre, C. Thieuleux, Chem. Commun. 46 (2010) 4722–4724.
[41] K. Moseley, P.M. Maitlis, J. Chem. Soc. D (1971) 982–983.
[42] P. Palmisano, N. Russo, P. Fino, D. Fino, Appl. Catal. B 69 (2006) 85–92.

[43] S. Specchia, E. Finocchio, G. Busca, G. Saracco, V. Specchia, Catal. Today 143 (2009) 86–93.
[44] Z. Yang, K. Zhou, X. Liu, Q. Tian, D. Lu, S. Yang, Nanotechnology 18 (2007) 185606.
[45] K. Pelzer, B. Laleu, F. Lefebvre, K. Philippot, B. Chaudret, J.P. Candy, J.M. Basset, Chem. Mater. 16 (2004) 4937–4941.
[46] F. Larachi, J. Pierre, A. Adnot, A. Bernis, Appl. Surf. Sci. 195 (2002) 236–250.
[47] E. Abi-aad, R. Bechara, J. Grimblot, A. Aboukaïs, Chem. Mater. 5 (1993) 793–797.
[48] J. Kugai, V. Subramani, C. Song, M.H. Engelhard, Y.-H. Chin, J. Catal. 238 (2006) 430–440.
[49] A.K. Sinha, K. Suzuki, J. Phys. Chem. B 109 (2005) 1708–1714.
[50] M. Machida, M. Uto, D. Kurogi, T. Kijima, Chem. Mater. 12 (2000) 3158–3164.
[51] J.-C. Dupin, D. Gonbeau, P. Vinatier, A. Levasseur, Phys. Chem. Chem. Phys. 2 (2000) 1319–1324.
[52] A. Mekki, D. Holland, Kh.A. Ziq, C.F. McConville, J. Non-Cryst. Solids 272 (2000) 179–190.
[53] C. Nethravathi, E.A. Anumol, M. Rajamathi, N. Ravishankar, Nanoscale 3 (2011) 569–571.
[54] Y. Nagai, H. Shinjoh, K. Yokota, Appl. Catal. B 39 (2002) 149–155.
[55] F. Grasset, P. Alphonse, C. Labrugère, J. Darriet, A. Rousset, Mater. Res. Bull. 34 (1999) 2101–2108.
[56] A.S. Aricò, A.K. Shukla, H. Kim, S. Park, M. Min, V. Antonucci, Appl. Surf. Sci. 172 (2001) 33–40.
[57] M. Piumetti, T. Andana, S. Bensaid, N. Russo, D. Fino, R. Pirone, Nanoscale Res. Lett. 11 (2016) 165.
[58] P. Mars, D.W. van Krevelen, Chem. Eng. Sci. 3 (1954) 41 (Spec. Suppl.).
[59] B.L.M. Hendriksen, M.D. Ackermann, R. van Rijn, D. Stoltz, I. Popa, O. Balmes, A. Resta, D. Wermeille, R. Felici, S. Ferrer, J.W.M. Frenken, Nat. Chem. 2 (2010) 730–734.
[60] B.V. L'vov, A.K. Galwey, J. Therm. Anal. Calorim. 111 (2013) 145–154.
[61] A. Erhan Aksoylu, M. Madalena, A. Freitas, J.L. Figueiredo, Catal. Today 62 (2000) 337–346.
[62] T.A. Nijhuis, M. Makkee, A.D. van Langeveld, J.A. Moulijn, Appl. Catal. A 164 (1997) 237–249.
[63] A. Moscu, Y. Schuurman, L. Veyre, C. Thieuleux, F. Meunier, Chem. Commun. 50 (2014) 8590.
[64] S.S. Mulla, N. Chen, L. Cumaranatunge, G.E. Blau, D.Y. Zemlyanov, W.N. Delgass, W.S. Epling, F.H. Ribeiro, J. Catal. 241 (2006) 389–399.
[65] H.-F. Wang, Y.-L. Guo, G. Lu, P. Hu, J. Phys. Chem. C 113 (2009) 18746–18752.
[66] C. Xu, B.E. Koel, Surf. Sci. 310 (1994) 198–208.
[67] A. Bueno-López, K. Krishna, B. van der Linden, G. Mul, J.A. Moulijn, M. Makkee, Catal. Today 121 (2007) 237–245.
[68] K. Balakrishnan, J. Schwank, J. Catal. 127 (1991) 287–306.
[69] A. Setiabudi, M. Makkee, J.A. Moulijn, Appl. Catal. B 50 (2004) 185–194.
[70] A. Setiabudi, J. Chen, G. Mul, M. Makkee, J.A. Moulijn, Appl. Catal. B 51 (2004) 9–19.
[71] Q. Shen, G. Lu, C. Du, Y. Guo, Y. Wang, Y. Guo, X. Gong, Chem. Eng. J. 218 (2013) 164–172.
[72] D. Baudouin, K.C. Szeto, P. Laurent, A. De Mallmann, B. Fenet, L. Veyre, U. Rodemerck, C. Copéret, C. Thieuleux, J. Am. Chem. Soc. 134 (2012) 20624–20627.
[73] http://www.xpsfitting.com/2012/01/silicon.html.
[74] Y. Nagai, T. Hirabayashi, K. Dohmae, N. Takagi, T. Minami, H. Shinjoh, S. Matsumoto, J. Catal. 242 (2006) 103–109.